Catalysis Today 437 (2024) 114585

Contents lists available at ScienceDirect

Catalysis Today

journal homepage: www.elsevier.com/locate/cattod

Impact of Co impregnation on 3D printed alumina supports for Fischer-Tropsch synthesis

Jasper Lefevere [a], Ben Sutens [a,*], Evert Boymans [b], Bart Michielsen [a]

[a] Flemish Institute for Technological Research – VITO, Boeretang 200, Mol B-2400, Belgium
[b] Netherlands Organisation for Applied Scientific Research – TNO, Westerduinweg 3, Petten 1755 LE, The Netherlands

ARTICLE INFO

Keywords:
3D printing
Catalyst preparation
Fischer-Tropsch

ABSTRACT

3D printing of catalyst has made a significant headway the past decade. Very often metal species on 3D printed supports are being used in catalysis. However, there is no standardized method of impregnation of 3D printed structures. In this work, the impact of the step in the production process where the impregnation is done was studied. Cobalt on alumina catalyst structures were synthesized using direct ink writing (DIW), characterized and tested in Fischer-Tropsch synthesis. Three different impregnation methods were tested (A) incipient wetness impregnation of the structure after printing (B) adding the metal salt precursor to the printing recipe and (C) impregnation of the alumina powder before printing. The catalysts exhibited significant differences in final properties, including pore volume in the fibers of the structure, cobalt nanoparticle size and metal-support interaction. When using the catalysts in Fischer-Tropsch synthesis, the activity of the catalyst impregnated after printing, was more than double the one with the metal salt in the print paste. The difference in conversion showed a clear correlation with the reducibility of the metal species measured with H_2-TPR.

1. Introduction

The world has known an unprecedented progress over the past century fueled by gas and oil. However, these fossil fuels have led to an increase in CO_2 emissions and heating of the planet [1]. Research focusses on replacing these fuels by alternative sources of power, for example in electric cars. Although this is very important, also alternatives are needed in sectors where liquid fuels cannot be replaced easily, such as aviation or maritime. For now, electric planes that run on batteries are not commercially viable due to their lower energy density. The conversion of alternative feedstocks, like biomass, into liquid fuels is therefore getting increasing attention. One of these processes of converting biomass in liquid fuels involves the production of syngas ($CO + H_2$) and subsequent Fischer-Tropsch synthesis (FTS). The products of the Fischer-Tropsch reaction include a wide range of hydrocarbons with different chain length, including various liquid fuels and waxes [2–5]. Usually, the heaviest products are put through a hydrocracking and refining process to increase the yield of the desired liquid fuels. In low temperature Fischer-Tropsch conversion reactions, cobalt on a support is typically used as catalyst in e.g. a packed bed reactor. These catalyst particles are usually in the range of 1–3 mm in diameter. A balance needs to be made between pressure drop and intraparticle diffusion limitations, which respectively increase and decrease with reducing particle diameters. In the past, work has been done to overcome this trade-off by using a thin coating of active catalyst on a monolith, foam or wire packing [6,7]. In general, low pressure drop and high catalyst effectiveness is obtained by using this strategy. However, the main drawback of these type of catalyst is their low catalyst loading per reactor volume and thus low productivity. In recent years, a new solution has come up to avoid the low loading in structured catalysts: directly 3D printing the catalyst [8–11].

For the past decade, additive manufacturing has been a hot topic as part of a greater push towards sustainability by improving the process efficiency and reducing the amount of raw materials needed significantly. Especially the chemical industry is a challenging sector to increase sustainability and reduce greenhouse gas emissions. Over the past years, several studies have been performed on the use of 3D printing as a functional tool for the chemical industry. Utilizing additive manufacturing for the production of reactors, static mixers and structured catalysts has been investigated for a wide range of different 3D printing techniques [12], including FDM, robocasting, stereolithography, inkjet printing, binder jetting, selective laser sintering and

* Corresponding author.
E-mail address: Ben.sutens@vito.be (B. Sutens).

https://doi.org/10.1016/j.cattod.2024.114585
Received 26 June 2023; Received in revised form 8 February 2024; Accepted 13 February 2024
Available online 21 February 2024

selective laser melting. Their use in chemical reactions have been extensively discussed in several review papers [12–15]. For the development of directly 3D printed catalytic structures, robocasting (also called Direct Ink Writing DIW) is considered as the most promising method [14]. In this technique, which was first described by Ceserano et al. in 1997 [16,17], a viscous paste is extruded through a thin nozzle. By computer-controlled movement of the nozzle, the structure is built up layer by layer according to the programmed design. Although other techniques allow for greater freedom of design, robocasting offers several advantages including the versatility in materials and the low amount of organic binder needed. Therefore, robocasting is considered as the preferred technique for 3D printing of structured catalysts. Moreover, it was shown that the architecture of the catalytic structure plays a significant role in the catalytic properties of the final material [18–20]. Other work showed the versatility of this technique by printing a wide array of materials for different catalytic reactions and sorption processes [8,10,21–25]. Most of the research involved direct printing of the active species including several types of MOFs and zeolites. However, only limited work has been done on the deposition of active metal species on a 3D printed support. Cepollaro et al. describe the introduction of Cu in a ZSM-5/geopolymer 3D printed structure for the NH_3-SCR of NOx. Copper acetate was used as precursor for copper ion exchange with the acidic zeolite. After ion-exchange, the samples were washed to remove the excess copper [26]. This type of impregnation procedure of the calcined 3D printed support was also used in other work [27,28]. An alernitive method was described by Tubio et al. A copper on alumina catalyst was synthesized by introducing the copper(II)nitrate precursor in the viscous paste. After sintering the printed structure at 1400°C, both alumina, CuO and copper aluminate spinel phases are formed. The final copper loading of the printed structures was equal to 2.35 w% and were subsequently used in different Ullmann reactions [9]. An additional method of introducing the metal species on a 3D printed support was described by Middelkoop et al. [29]. Nickel nitrate precursor was impregnated on alumina powder prior to the printing process. After freeze drying and milling of the prepared Ni on alumina, the powder was used to prepare a viscous ink. A calcination step at 500 °C was performed after 3D printing, resulting in a 12 w% Ni on alumina as a catalyst for CO_2 methanation. A similar method was used by Jacquot et al. [30]. Up till now, one single study has been performed on the impact of the impregnation method on the physico-chemical and catalytic properties of 3D printed structures. Elkoro et al. studied the impact of Au impregnation on titania before and after printing for hydrogen photoproduction [31]. The post-impregnation method showed 2–3 orders of magnitude higher production rate compared to the pre-impregnation route, as the Au particles were only deposited on the outside of the structure in the post impregnation route. The lack of porosity in the fibers of the structure resulted the Au inside of the fibers to be inaccessible using the pre-impregnation route.

In this work, the impact of the impregnation method on the catalytic performance was evaluated in the case of the Fischer-Tropsch reaction. It is known that the overall catalytic performance is greatly affected by the cobalt concentration, the nanoparticle size and the nature of the support. Since the impregnation method can have a large influence on these properties, highly porous γ-Al_2O_3 supported cobalt catalysts were developed by using various impregnation methods. Three different methods were explored by introducing the cobalt precursor at different stages in the manufacturing process of the 3D printed catalyst. Subsequently, the effect of the impregnation method on the porosity, catalyst crystal size, homogeneity of the dispersion and the catalytic activity was evaluated by N_2 sorption, Hg porosimetry, XRD, SEM and catalytic tests in a pilot-scale reactor.

2. Materials and methods

The γ-Al_2O_3 supported Cobalt catalysts were developed by combining a γ-Al_2O_3 precursor (Puralox TH 100/150; Sasol) and a Cobalt salt ($Co(NO_3)2$. H_2O, Merck) as precursor for the metal species. Disperal P2 (Sasol) was added as a permanent binder in a 20 w% ratio relative to Puralox to provide sufficient mechanical strength after calcination. As a rheology modifier, methyl cellulose (Merck) was used to achieve the appropriate viscosity for printing. The different inks were prepared by mixing the respective components in a centrifugal mixer (Thinky ARE-250) for 2 minutes at 1900 rpm. The paste was allowed to cool down for 1 h at 4 °C before being transferred to a plexiglass container.

All samples were printed using an 800 μm nozzle with 800 μm spacing between the deposited fibers using direct ink writing, resulting in cylindrical monolithic-type structures of 3 cm height and 3 cm diameter. After printing, the structures were dried at room temperature for 2 days, followed by a thermal treatment of 3 h at 550 °C to remove the organic binder. Three different impregnation methods were explored by introducing the cobalt precursor at different stages in the manufacturing process of the 3D printed catalyst (Fig. 1), including (A) incipient wetness impregnation after printing and calcination of the alumina support, (B) addition of the cobalt salt directly into the alumina and water containing viscous paste and (C) incipient wetness impregnation on the Puralox starting powder. To remove the nitrates from the Co precursor, an additional calcination step for 2 h at 250°C was introduced after impregnation. All samples were prepared to end up with a final Co concentration of 7.5 w%. Prior to catalytic testing, samples were crushed and sieved to the appropriate particle size range of 200–400 μm.

2.1. Characterization

The rheological properties of the inks were measured using a rotational rheometer (Haake Rheowin MARS 60, Thermofisher Ltd., Germany) fitted with a parallel plate geometry (PP35Ti, diameter of 35 mm and gap of 0.4 mm) at 25 °C. The shear elastic modulus (G′) and viscous modulus (G") were measured with an oscillatory logarithmic stress sweep between 1 and 10,000 Pa at the frequency of 1 Hz.

After preparation of the samples, the porosity in the fibers of the structure was determined using nitrogen sorption and mercury porosimetry. The nitrogen sorption measurement was performed on a Quantachrome Autosorb iQ in order to determine the specific surface area and pore volume. The Brunauer-Emmett-Teller (BET) method was used to calculate the specific surface area. Pore volume was calculated by using the BJH method. Prior to measurement, the samples were degassed for 16 h at 200°C. The Hg porosimetry was performed on a Pascal Mercury porosimeter (Thermo Scientific) to measure pore radius between 3.8 nm and 75 μm. X-ray diffraction (Philips/Pnanlytical X'Pert Pro diffractometer) was applied to determine the phase and crystallinity of the manufactured samples using a Cu-K_α X-ray source ($\lambda = 0.15418$ nm). Phase identification was done using X'Pert High Score Plus software and compared to reference data in the ICDD powder Diffraction database. The size of the cobalt nanoparticles on the alumina support was estimated using the XRD peak at 43° of CoO. For visualization of the samples, Scanning Electron microscopy (SEM) (FEGFEI Nova NanoSEM 450) was used at an accelerating voltage of 5 kV. The distribution of the different elements was measured using energy dispersive X-ray (EDX) spectroscopy (QUANTAX 200 EDX, Bruker with an XFlash 5030 SDD detector). The exact amount of cobalt on the alumina samples was determined by using inductively coupled plasma- atomic emission spectroscopy (ICP) on a Perkin-Elmer Optima 3000 device. Temperature programmed reduction (TPR) was performed using a Quantachrome Atosorb iQ with a TCD detector. Before TPR samples were oxidized under a 5 % O_2 in He gas stream at 200 °C and subsequently cooled down to 30 °C. The TPR measurement occurred under a flow of 5% H_2 in Ar at a flow rate of 30 ml/min and heating at 10 °C/min to 1000°C. The samples were investigated by Optical Microscopy using a Zeiss Discovery V12 Stereomicroscope, equipped with a Plan Apo S 1.0xFWD 60 mm objective. Images are taken by an Axiovision MRc digital camera

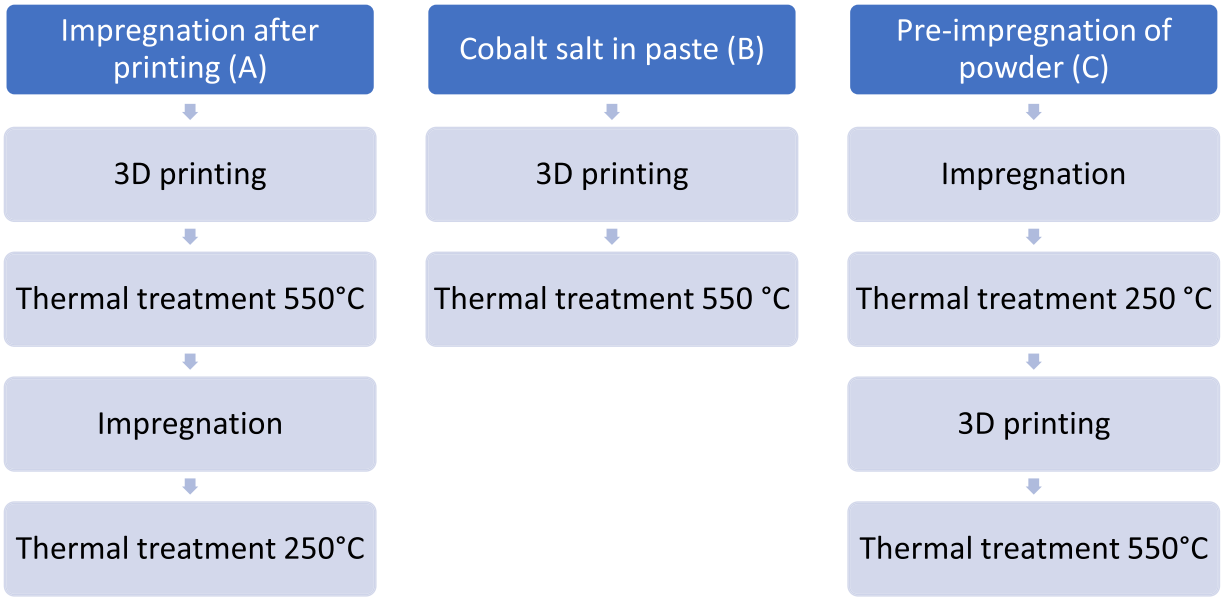

Fig. 1. Process steps in the different impregnation methods for 3D printed Cobalt on alumina catalyst, resp. A, B and C.

connected to the microscope. The fibre diameter was determined using the ZEN3.2 (Zeiss) software.

2.2. Catalytic testing

The catalytic testing on the powder of the crushed monoliths was performed in a micro-flow reactor unit with 4 parallel reactor tubes, see also Fig. 2. These reactor tubes are placed in a single heated block to run under identical conditions i.e., feed composition, flow, temperature, pressure and gas/liquid separation. Where the flow of the required gas mixture is set using a Coriolis mass-flow controller. Condensation of the wax and light hydrocarbons from the reactor outlet gas occurs in respectively a hot (170°C) and cold (5°C) separator at the reactor pressure. The stainless-steel reactor tubes have an inner diameter of 8 mm, and a 10 cm long isothermal zone with a 3-point thermocouple in the center line. Mixtures of 1.5 g catalyst and 9 g α-alumina (inert) were placed in the isothermal zone of each reactor tube for the catalytic runs. All catalysts were activated by introducing 50 vol% H_2 in N_2 at 1 barg at 340 °C for 1 h at 1 °C/min and a WHSV of 3.3 $g_{gas}g_{cat}^{-1}h^{-1}$. For setting the reference reaction conditions, consecutively, the reactors were allowed to cool to 220°C, the flow was set to 2.0 $g_{gas}g_{cat}^{-1}h^{-1}$, the pressure was set to 20 barg, followed by slow (3 h) introduction of CO to reach the desired gas composition of 32 vol% CO, 63 vol% H_2 and 5 vol% N_2. Gas analysis results were obtained under pseudo steady-state conditions at least 15 h after the desired reaction conditions were established. Gas samples from each reactor were withdrawn downstream the hot separators. The gases were measured using an online GC equipped with separate channels for the detection of N_2, Ar, CO_2, CH_4, CO (HS-N column with TCD detector), H_2 (Molsieve 5A column 388 with TCD detector) and C_1-C_4 (PlotQ column with FID detector).

Conversion and selectivity were calculated based on the following expressions:

$$X_{CO}\,[C\%] = (F_{CO,\,in} - F_{CO,\,out})/\,F_{CO,\,in} * 100\%$$

$$S_{Cn}\,[C\%] = F_{Cn} / (F_{CO,\,in} - F_{CO,\,out}) * 100\%$$

$$S_{C5+}\,[C\%] = 100\% - \Sigma\, S_{C1\text{-}C4}$$

Where X_{CO} is the CO conversion in % and F_{CO} is the molar carbon flow of CO. S_{Cn} represents the carbon selectivity to all components with n carbon atoms with F_{Cn} the corresponding molar carbon flow. Finally, S_{C5+} defines the liquid carbon selectivity.

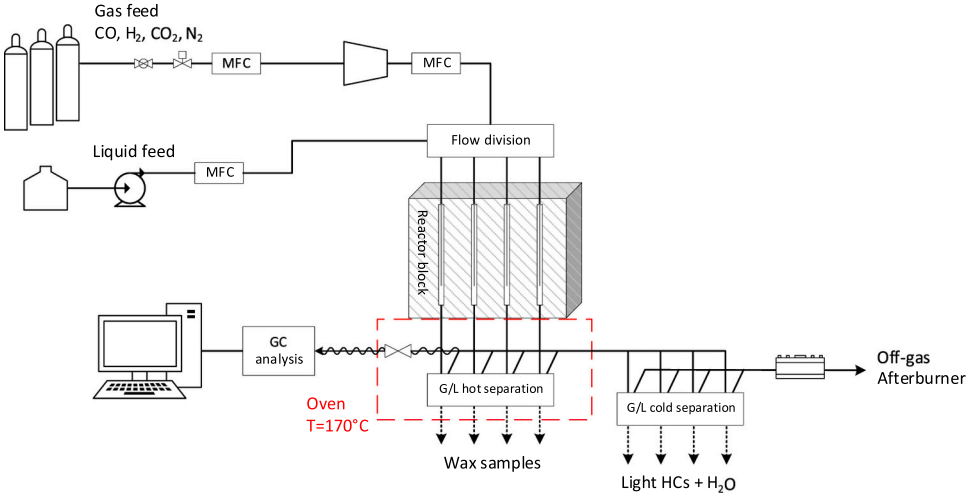

Fig. 2. The micro-flow reactor setup used in the catalytic FT experiments.

3. Results

3.1. 3D printing & physicochemical properties

The different impregnation procedures are shown in Fig. 1. Already, there was a clear impact on the formulation using the different impregnation methods. In order to reach the rheology suitable for printing, the amount of water in the viscous paste of each formulation was different. When comparing the pure alumina powder formulation with the one using pre-impregnated powder, the powder loading of the Co/Al_2O_3 powder was lower. Although this powder has a higher density by adding the cobalt onto the alumina, the amount of water needed for a printable paste was significantly increased. This might be caused by a higher water demand for internal wetting of the material due to the cobalt nanoparticles present. This reduces the water in between the alumina particles resulting in a higher amount of water needed in the formulation. In the case of the use of the cobalt salt in the paste, the alumina to water ratio was even lower. All the cobalt ions present in the formulation claim water to develop the hydration shell, increasing the water content is needed to obtain a printable paste. Furthermore, the addition of the cobalt nitrate could result in an alteration of the pH of the paste. From zeta potential measurements of alumina in aqueous suspensions, it is known that pH has a large influence on the surface charge of the alumina powder and thus the repulsion between particles and powder loading possible [32].

The percentage of alumina solids in the printing pastes was equal to 51.2 (A), 36.0 (B) and 44.8 (C) w% for respectively the pure alumina paste, impregnation in the paste and the pre-impregnated powder formulations.

The amplitude swing measurements (Fig. 3) show that despite having the highest moisture content, the formulation with the cobalt in the paste exhibited the highest rigidity and viscosity in rest, as the storage modulus (G') and loss modulus (G'') are significantly higher in comparison with the other formulations. Also, the flow point, being the point at which G' and G'' cross, is slightly higher for the formulation with the cobalt nitrate in the paste compared to the pure alumina paste. This indicates that a slightly higher strength will be needed to induce the pastes to flow. The sample with the impregnated powder shows the lowest viscosity in rest and needs the lowest force to be extruded. In order to reach similar viscosity compared to the other pastes, the powder loading in this paste could be slightly increased. All pastes were printable, Fig. 4 shows a picture of the 3D printed structure using the metal precursor in the printing paste, after drying before calcination.

The powder loading in the formulation of the paste can directly be correlated to the pore volume of the different samples. The Mercury porosimetry shown in Fig. 5 shows that the sample with the lowest powder loading yields the highest meso-macro porosity. Interestingly, for the sample with the cobalt salt in the paste, the pore size distribution is different compared to the other 2 samples. Although a bimodal porosity is still observed, the large pores have a diameter of around 2–3 μm whereas for the pure alumina impregnated after printing and the structure from the pre-impregnated powder, the larger pores are observed around 0.7 μm. For all samples, the largest amount of pore volume can be found around 0.01 μm. Since the bottom part of the curve is close to the detection limit of Mercury porosimetry, it is very likely

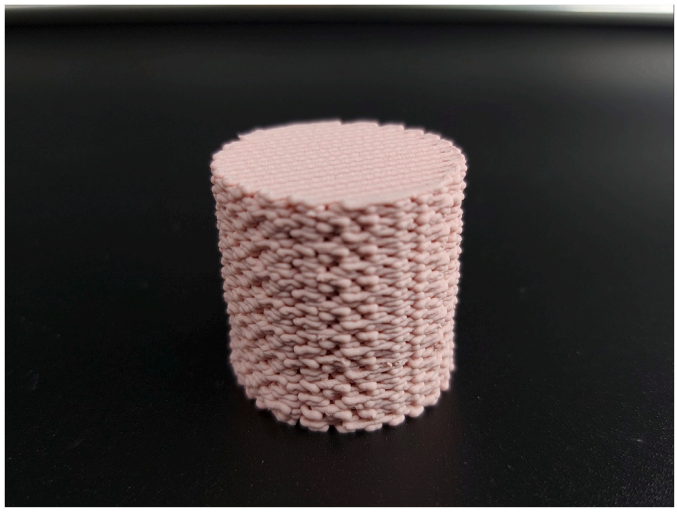

Fig. 4. Picture of 3D printed structure with cobalt salt in the paste after printing, before calcination.

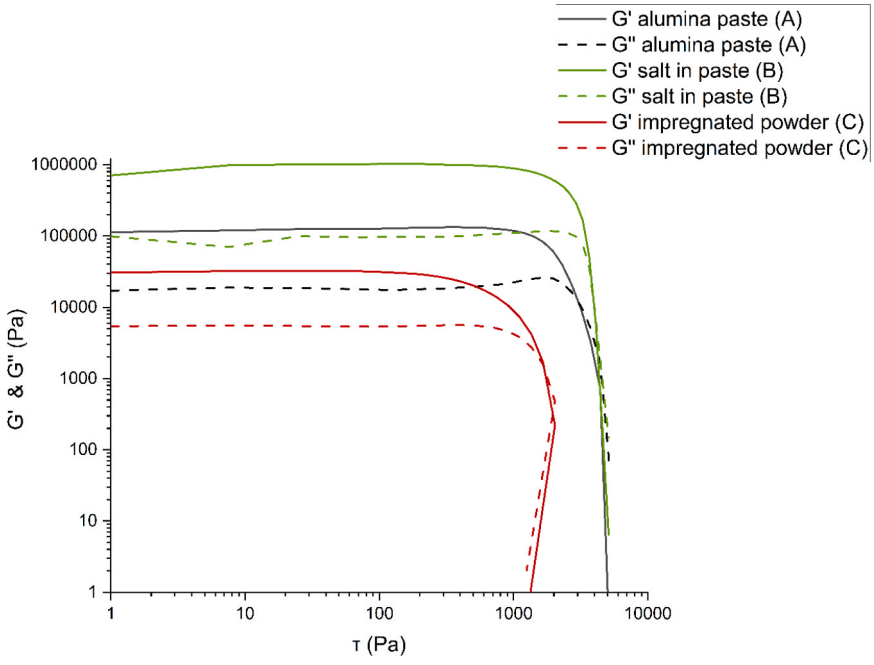

Fig. 3. Rheology measurement of the different formulations. Storage modulus G' and loss modulus G'' in function of shear stress τ.

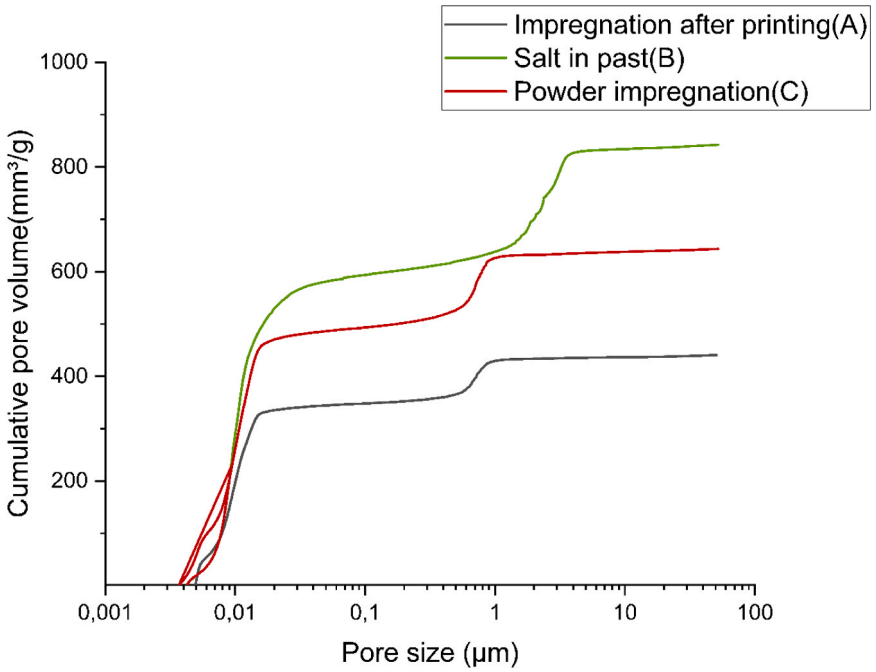

Fig. 5. Mercury porosimetry of the structures made with the different impregnation methods.

that this is an underestimation of the pore volume. Therefore, Nitrogen sorption measurements have been performed to analyze the complete porosity spectrum.

The results of nitrogen sorption show no significant differences between the samples in terms of surface area (Table 1). As was expected, the surface area per gram is slightly reduced after impregnation due to the increased density of the material. The calculated mesopore volume (< 50 nm) is slightly higher in comparison with the results based on Hg porosimetry, since also the pores smaller than 7 nm are measured with nitrogen sorption. The data confirm the trend in pore volume between the samples, with the structure made with the cobalt salt in the paste having the highest porosity and the structure impregnated after printing exhibiting the lowest porosity.

XRD analysis (Fig. 6) shows a clear difference between the impregnated materials compared to the pure alumina structure. As observed, the main peaks of cobalt correspond to the Co_3O_4-phase present on the alumina support. Further investigation shows that the peaks demonstrate an increased intensity and sharpness for the sample prepared with pre-impregnated powder. The formulation made with the cobalt salt in the paste showed the lowest intensity of Co_3O_4 peaks in the XRD pattern. Based on the peak at an angle of 43°, the nanoparticle size was calculated. The Co crystal size of the samples with pre-impregnated powder, impregnated after printing and the salt in the paste were equal to 10.90 (A), 7.43 nm (B) and 23.77 (C) respectively. ICP analysis (supplementary information table s1) confirmed that there was no significant difference in concentration of Co in the samples.

Optic and electron microscopy (supplementary information Figs. 1s & 2s) were used to visualize the samples. Optic microscopy shows a very regular structure for all the manufacturing methods. SEM indicates that the surface roughness and porosity in the fibers of the samples is different. In line with the Hg-porosimetry, the structure with the salt in the paste shows the highest porosity in the fiber and roughness of the surface.

The distribution of the cobalt throughout the fibers was visualized using EDX (Fig. 2s). A homogenous distribution is observed in case of the samples developed by addition of the cobalt salt to the paste as well as post-impregnation after printing. The location of the cobalt correlates with the location of alumina. The sample made from the impregnated powder shows more brighter spots, which can be correlated to the larger nanoparticle size of the Co_3O_4. The larger nanoparticles might be caused by the higher concentration of cobalt in the lower volume of pores of the powder in comparison with the higher volume of porosity in between the alumina particles and the binder for the other impregnation methods. In contrast with the work of Elkoro et al. [31], where the post impregnation method yielded a catalyst with the Au nanoparticles only on the outer surface, the cobalt nanoparticles in this work are homogenously distributed due to the porosity in the fiber.

To activate the catalysts and reduce the Co_3O_4 to Co a reduction step before reaction is needed. Temperature programmed reduction (TPR) shown in Fig. 7 indicates the reduction temperature of the different samples under H_2 atmosphere. Clearly, the synthesis route has a large impact on the reduction profile. This indicates that the metal-support interactions are different between the structures. The Co impregnated after printing (C) showed a reduction peak at the lowest temperature, around 275 °C and a second peak around 425 °C. The structure of pre-impregnated powder on the other hand, showed just a single peak around 350 °C. Lastly, the structure produced with the cobalt salt in the paste (B) showed the strongest metal-support interactions with peaks at different temperatures, but in general reduction only at elevated temperatures.

The differences in the impregnation method and sequence of calcination steps lead to changes in porosity, metal nanoparticle size and metal support interaction. Reasons for this could be the different calcination temperature the cobalt undergoes, in method B and C this is 550 °C whereas if the structure is impregnated after printing (A) the cobalt only gets exposed to a temperature of 250 °C for calcination. However,

Table 1
Results of nitrogen sorption and XRD analysis.

Sample	BET (m^2/g)	Pore volume (<50 nm) (ml/g)	Crystal size (nm)
Alumina before impregnation	172	0.61	/
Impregnation after printing (A)	158	0.54	10.9
Salt in paste (B)	150	0.72	7.43
Powder impregnation (C)	146	0.61	23.77

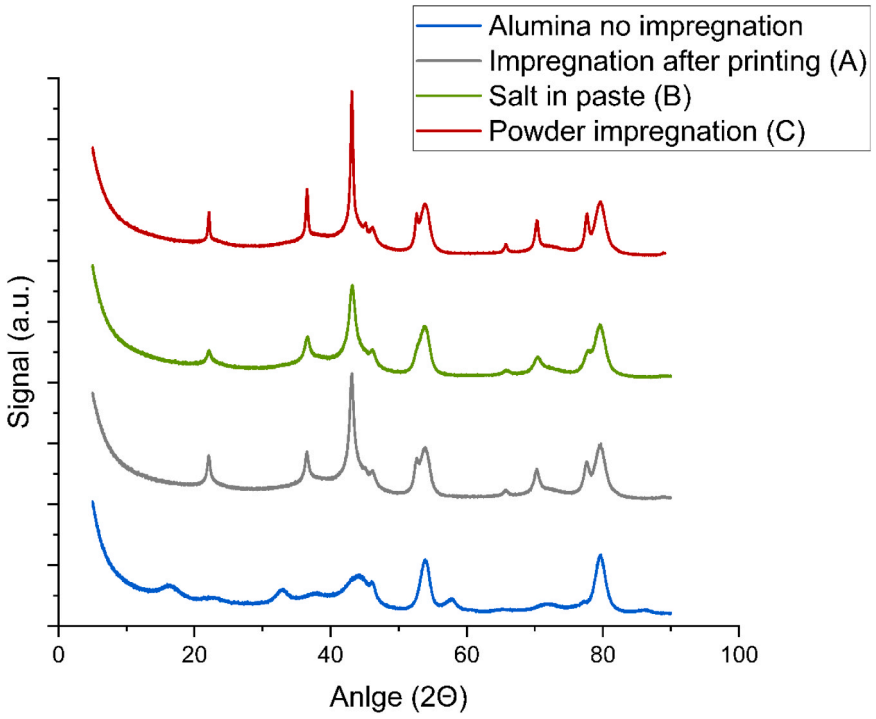

Fig. 6. XRD pattern of alumina and structures manufactured with the different impregnation methods.

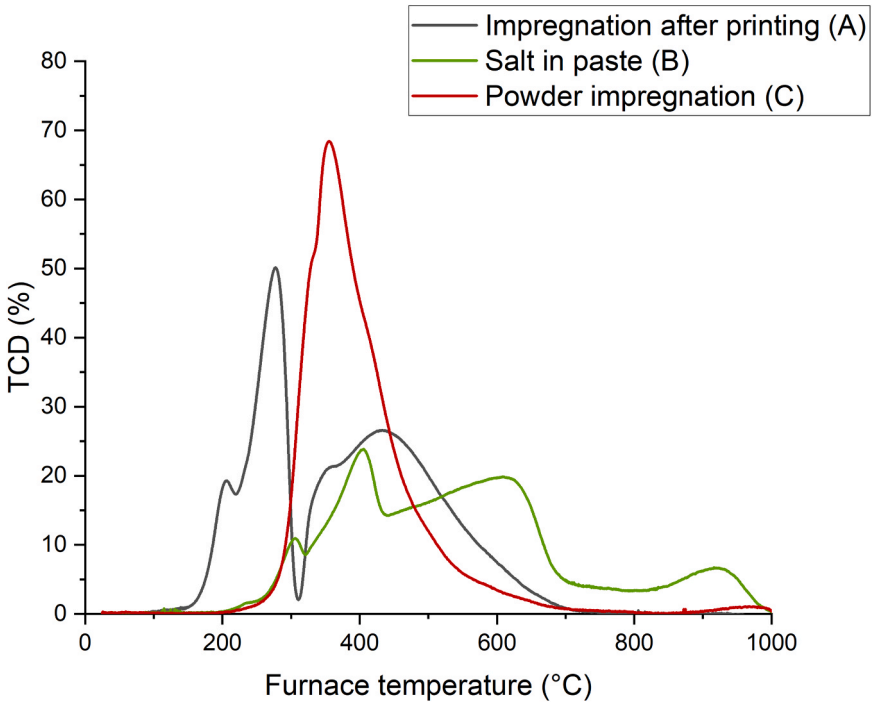

Fig. 7. H_2-TPR measurement for the samples with different impregnation method.

temperature alone cannot explain the different behavior as the method B, with the metal salt in the paste, shows the smallest nanoparticle size although it has been treated at 550 °C. A reason for the low particle size and strong interaction with the support in method B might be that this method is the only one where the cobalt precursor comes in contact with the boehmite binder. As this binder has a lot of hydroxyl groups, there can be a strong interaction with the cobalt nitrate. Upon calcination the hydroxyl groups condensate, gamma alumina is formed and bind with the other alumina, this process might lead to a strong bonding between the metal and alumina and prevent crystal growth.

3.2. *Catalytic testing*

Catalytic testing of all three crushed catalysts under FT conditions at 220 °C and 240 °C showed the impact of the synthesis routes on catalyst activity and selectivity, see Table 2. Catalyst B (salt in paste) resulted in

Table 2
Catalytic results of Fischer-Tropsch synthesis at 220°C and 240°C for the catalysts manufactured with different impregnation methods.

	TOS	X_{CO}	CTY/10^{-5}	C Selectivity [C%]		
	[h]	[%]	[mol_{CO} g_{Co}^{-1} s^{-1}]	CH_4	C_{5+}	CO_2
(A, post) 220 °C	36	20.5	4.2	9.8	82.2	0.1
(A) 220 °C	180	25.4	5.2	7.4	84.7	0.1
(A) 240 °C	84	49.3	20.3	11.9	77.1	0.3
(B, in paste) 220 °C	73	9.7	2.0	10.1	81.7	0.0
(B) 220 °C	336	13.5	2.8	11.3	81.9	0.2
(B) 240 °C	119	17.4	7.3	13.4	78.7	0.2
(C, on powder) 220 °C	74	17.2	3.5	9.3	84.2	0.2
(C) 220 °C	337	16.8	3.4	10.2	82.2	0.1
(C) 240 °C	120	31.7	12.9	12.4	79.5	0.2

Note: WHSV = 2 g_{gas} g_{cat} h^{-1} (220 °C) and 4 g_{gas} g_{cat} h^{-1} (240 °C), P = 20 barg, inlet gas composition: 32 vol% CO, 63 vol% H_2, 5 vol% N_2.

the lowest activity (cobalt-time-yield, CTY) of the tested catalysts. This might be caused by the different interaction between the cobalt and the support or the different impregnation methods. As the reduction before reaction is performed at 340 °C, only a small portion of the cobalt oxide might have been reduced. The TPR measurement has shown that the sample with cobalt in the paste has the highest reduction temperature, only a small peak below 340 °C can be observed. Performing the impregnation step after printing, resulted in the highest amount of cobalt reduced below 340°C followed by the pre-impregnation of the powder, which is in line with the activity of the catalyst. Catalyst A (post-impregnation) exhibited the highest conversion which can be correlated to the higher reducibility at 340 °C. The selectivity of all the catalysts was in the same range. Work by Borg et al. [33] shows that there is a correlation between cobalt nanoparticle size and the selectivity towards C_{5+}. Larger cobalt nanoparticle size leads to higher selectivity of C_{5+}. Although in our work this is not clearly the case, post mortem analysis should be performed in future work to evaluated the effective nanoparticle size in reaction conditions. At higher temperature the activity of all catalysts increases, while the selectivity towards C_{5+} decreases. This is in line with literature [3,34]. The difference in pore volume does not seem to have an influence on the activity or selectivity in this catalytic testing. However, literature suggest that in shaped pellets this might be of importance [35]. An abundance of macropores in larger catalyst pellets showed a beneficial result in FT synthesis. As the catalyst is tested as granules (200–400 μm) in this work, this effect could not be observed. Whereas in the work of Elkoro et al. the difference in activity between the two different impregnation methods of 3D printed structures could be attributed to the location of the nanoparticles, this is not the case with these Co catalysts [31]. The difference in this work can be attributed to the reactivity of the nanoparticles itself due to the interaction between support and nanoparticles. As in the three impregnation methods, most the cobalt nanoparticles were available for reaction, in contrast with the work of Elkoro, the difference in activity of the synthesized catalysts was smaller compared to the 2–3 orders of magnitude reported in that work. Finally, the activity and selectivity of the catalysts were re-established after prolonged time-on-stream (TOS) under identical conditions to determine their stability. For the post-impregnated catalyst A, the CTY slightly increased from 4.2 s^{-1} (36 h) to 5.2 s^{-1} (180 h) at 220 °C. This can again be attributed to the Co oxide particles that continued to be reduced and activated during the FT experiment runs. The same trend was obtained with catalyst B, whereas catalyst C retained its activity.

4. Conclusions

Fischer-Tropsch catalysts were prepared using robocasting and three different impregnation methods. At different steps in the production process, cobalt was added to the alumina support material: after printing, during the mixing of the paste and before printing on the powder. The physio-chemical properties of the materials were significantly influenced by the impregnation method. The macropore volume, nanoparticle size and interaction between the cobalt and the support material were different for the three impregnation methods. These different properties influenced the catalytic properties of the different materials in the FT process. The activity of the catalyst was mainly influenced by the metal-support interaction. With increasingly stronger interaction, the reduction temperature of the cobalt did go up and activity went down. Impregnation after printing showed the highest activity whereas the activity was lowest when the cobalt salt was mixed in the print paste. A slight difference in selectivity could be attributed to the difference in cobalt nanoparticle size.

3D printing is a useful tool to manufacture catalysts however, this work has shown that it is important to consider the impregnation method and its location in the production process. It is possible to tune the properties of the catalyst by using this parameter. In future work the impact on stability should also be investigated, as well as the usability of this findings towards other supports, metals and reactions. Furthermore, this optimized impregnation method will be used to tests the properties of structured catalysts in comparison with traditional pellets in a larger scale Fischer -Tropsch reactor.

CRediT authorship contribution statement

Jasper Lefevere: Writing – original draft, Project administration, Methodology, Investigation, Formal analysis, Conceptualization. **Bart Michielsen:** Writing – review & editing, Conceptualization. **Ben Sutens:** Writing – review & editing, Investigation, Formal analysis, Data curation. **Evert Boymans:** Writing – review & editing, Project administration, Investigation, Formal analysis, Data curation.

Declaration of Competing Interest

The authors declare that they have no known competing financial interests or personal relationships that could have appeared to influence the work reported in this paper.

Data availability

Data will be made available on request.

Acknowledgment

The authors would like to thank Karen Leyssens and Vera Meynen of the LADCA group of the University of Antwerp for the TPR measurements and Raymond Kemps, Annemie De Wilde and Myrjam Mertens from VITO for the SEM, N_2-sorption, Hg porosimetry and XRD measurements. This work is part of the GLAMOUR project which is supported by the European Union's Horizon 2020 Research And Innovation Programme under grant agreement No 884197.

Appendix A. Supporting information

Supplementary data associated with this article can be found in the online version at doi:10.1016/j.cattod.2024.114585.

References

[1] T.L. Frölicher, M. Winton, J.L. Sarmiento, Nat. Clim. Chang 4 (2014) 40–44.
[2] R. Guettel, U. Kunz, T. Turek, Chem. Eng. Technol. 31 (2008) 746–754.
[3] E. Iglesia, Appl. Catal. A Gen. 161 (1997) 59–78.
[4] L.U. Okonye, Y. Yao, D. Hildebrandt, R. Meijboom, Sustain. Energy Fuels 5 (2021) 79–107.
[5] Z. Gholami, Z. Tišler, V. Rubáš, Catal. Rev. Sci. Eng. 63 (2021) 512–595.

[6] M. Ibáñez, O. Sanz, A. Egaña, I. Reyero, F. Bimbela, L.M. Gandía, M. Montes, Chem. Eng. J. 425 (2021) 130424.
[7] L. Fratalocchi, G. Groppi, C.G. Visconti, L. Lietti, E. Tronconi, Chem. Eng. J. 386 (2020) 123988.
[8] C. Parra-Cabrera, C. Achille, S. Kuhn, R. Ameloot, Chem. Soc. Rev. 47 (2018) 209–230.
[9] C.R. Tubío, J. Azuaje, L. Escalante, A. Coelho, F. Guitián, E. Sotelo, A. Gil, J. Catal. 334 (2016) 110–115.
[10] M. Konarova, G. Jones, V. Rudolph, Results Eng. 6 (2020) 100127.
[11] J. Lefevere, S. Mullens, V. Meynen, Chem. Eng. J. 349 (2018) 260–268.
[12] C. Parra-Cabrera, C. Achille, S. Kuhn, R. Ameloot, Chem. Soc. Rev. (2017) 1–35.
[13] Z. Chen, Z. Li, J. Li, C. Liu, C. Lao, Y. Fu, C. Liu, Y. Li, P. Wang, Y. He, J. Eur. Ceram. Soc. 39 (2019) 661–687.
[14] S. Lawson, X. Li, H. Thakkar, A.A. Rownaghi, F. Rezaei, Chem. Rev. 121 (2021) 6246–6291.
[15] X. Zhou, C. Liu, Adv. Funct. Mater. 27 (2017) 1701134.
[16] J. Cesarano, S. Grieco, Mater. Technol. 12 (1997) 98–100.
[17] J.N. Stuecker, J.E. Miller, R.E. Ferrizz, J.E. Mudd, J. Cesarano, Ind. Eng. Chem. Res. 43 (2004) 51–55.
[18] J. Lefevere, L. Protasova, S. Mullens, V. Meynen, Mater. Des. 134 (2017) 331–341.
[19] J. Lefevere, S. Mullens, V. Meynen, Chem. Eng. J. 349 (2018) 260–268.
[20] J. Lefevere, M. Gysen, S. Mullens, V. Meynen, J. Van Noyen, Catal. Today 216 (2013) 18–23.
[21] S. Lawson, X. Li, H. Thakkar, A.A. Rownaghi, F. Rezaei, Chem. Rev. 121 (2021) 6246–6291.
[22] S. Danaci, L. Protasova, J. Lefevere, L. Bedel, R. Guilet, P. Marty, Catal. Today 273 (2016) 234–243.
[23] J. Lefevere, B. Claessens, S. Mullens, G. Baron, J. Cousin-Saint-Remi and J.F.M. Denayer, ACS Appl. Nano Mater., ⟨doi:10.1021/acsanm.9b00934⟩.
[24] B. Claessens, N. Dubois, J. Lefevere, S. Mullens, J. Cousin-Saint-Remi, J.F. M. Denayer, Ind. Eng. Chem. Res. 59 (2020) 8813–8824.
[25] S. Couck, J. Lefevere, S. Mullens, L. Protasova, V. Meynen, G. Desmet, G.V. Baron, J.F.M. Denayer, Chem. Eng. J. 308 (2017) 719–726.
[26] E.M. Cepollaro, R. Botti, G. Franchin, L. Lisi, P. Colombo and S. Cimino, Catalysts, ⟨doi:10.3390/catal11101212⟩.
[27] I. Lucentini, I. Serrano, L. Soler, N.J. Divins and J. Llorca, Appl. Catal. A Gen., ⟨doi:10.1016/j.apcata.2019.117382⟩.
[28] I. Lucentini, G. García Colli, C. Luzi, I. Serrano, L. Soler, N.J. Divins, O.M. Martínez and J. Llorca, Chem. Eng. J., ⟨doi:10.1016/j.cej.2021.131756⟩.
[29] V. Middelkoop, A. Vamvakeros, D. De Wit, S.D.M. Jacques, S. Danaci, C. Jacquot, Y. De Vos, D. Matras, S.W.T. Price, A.M. Beale, J. CO2 Util. 33 (2019) 478–487.
[30] C. Jacquot, V. Middelkoop, A. Köckritz, A. Pohar, R. Bienert, S. Kellici, I.A. Bărăgău, B. Venezia, A. Gavriilidis, B. Likozar and A.M. Beale, Sustain. Mater. Technol., ⟨doi:10.1016/j.susmat.2021.e00329⟩.
[31] A. Elkoro, L. Soler, J. Llorca, I. Casanova, Appl. Mater. Today 16 (2019) 265–272.
[32] R. Sprycha, Electr. Double Layer. Alumina/Electrolyte Interface I. Surf. Charg. Zeta Potential (1989).
[33] Ø. Borg, P.D.C. Dietzel, A.I. Spjelkavik, E.Z. Tveten, J.C. Walmsley, S. Diplas, S. Eri, A. Holmen, E. Rytter, J. Catal. 259 (2008) 161–164.
[34] N.E. Tsakoumis, M. Rønning, Ø. Borg, E. Rytter, A. Holmen, Catal. Today 154 (2010) 162–182.
[35] H. Li, J. Wang, C. Chen, L. Jia, B. Hou, D. Li, RSC Adv. 7 (2017) 9436–9445.